Wave spectrum retrieval from airborne sunglitter images

Maria Yurovskaya, Nicolas Rascle, Vladimir Kudryavtsev, Bertrand Chapron, Louis Marie, Jeroen Molemaker

Remote Sensing Of Environment
November 2018, Volume 217 Pages 61-71
https://doi.org/10.1016/j.rse.2018.07.026
https://archimer.ifremer.fr/doc/00465/57712/

Wave spectrum retrieval from airborne sunglitter images

Yurovskaya Maria [1, 2, *], Rascle Nicolas [3, 4], Kudryavtsev Vladimir [1, 2], Chapron Bertrand [2, 4], Marie Louis [4], Molemaker Jeroen [4]

[1] RAS, Marine Hydrophys Inst, Sevastopol, Russia.
[2] Russian State Hydrometeorol Univ, Satellite Oceanog Lab, St Petersburg, Russia.
[3] Ctr Invest Cient & Educ Super Ensenada, Div Oceanol, Ensenada, Baja California, Mexico.
[4] Inst Francais Rech Exploitat Mer, Plouzane, France.

* Corresponding author : Maria Yurovskaya, email address : mvkosnik@gmail.com

Abstract :

Reconstruction and evolution of two-dimensional spectra of surface waves in the Gulf of Mexico are derived from airborne sun-glitter imagery. As the proposed method is based on a linear transfer function deduced from the shape of the sunglitter brightness, the absolute wavenumber elevation spectrum does not require any additional assumption or information about sky brightness, wind or wave energy. The detailed description of the airborne image processing method is given. As demonstrated, retrieved spectra agree well with nearby NDBC buoy data, both for spectrum shape, level and energy angular distribution. The 180-degree wave direction ambiguity, inherent to image-derived spectra, is eliminated by using cross-correlation analysis between two consecutive images. A case study corresponding to the spectral evolution with increasing distance from shore in slanting fetch conditions is then considered. Energy level and peak position transformation are consistent with established approximations and laws of wind-sea development. The technical requirements (flight altitude, image resolution, view angles, etc) and applicability of the suggested methodology are also discussed. These results demonstrate the potential efficiency of high resolution sea state monitoring from drones or light aircrafts using sunglitter imagery.

Highlights

► Sea surface wave spectra are derived from airborne sunglitter imagery. ► A linear transfer function relates sunglitter brightness and wave elevation spectra. ► The method is applied to airborne images taken in the Gulf of Mexico. ► A case study on the spectral evolution with fetch increasing is considered. ► The technical requirements and method applicability are discussed.

Keywords : Sunglitter, Sea surface waves, Directional wave spectrum, Aerial photography, Field measurements, Remote sensing observations, High resolution, Drone

1. Introduction

For a wide range of applications, such as coastal management, the design and operational safety of harbours, ships, and offshore structures, a precise knowledge of the directional spectrum of ocean waves is needed. The directional wave spectrum describes the distributed energy contributions from waves propagating in different directions with different wavelengths. It is key to help determine the consequences of interactions between waves and other structures, i.e. breakwaters and offshore structures, but also to evaluate

wave-induced upper ocean transport and erosion processes.

Significant advances have thus been made to estimate these directional wave statistical properties. Today, a large number of measuring devices, working on different principles, are available (e.g. Herbers et al., 2012). Yet, the directional and frequency response of these systems may often be limited and not sufficient to fully resolve directional surface wave spectra. Further, requirements for near-simultaneous, high spatial resolution observations, to provide more direct directional wavenumber measurements of the local surface field over entire regions, has attracted the attention on remote sensing technologies. To complement sparse in-situ buoy measurements, techniques can include sea level radars (coastal HF radars, Barrick and Lipa, 1985), microwave and marine X-band radars (Senet et al., 2008; Nieto et al., 2004), scanning altimeter and lidar high-resolution topography instruments from airplane platforms (Walsh et al., 1998; Melville et al., 2016), and also synthetic aperture or rotating real-aperture airborne radar instruments (Caudal et al., 2014). As well, photographs of the ocean surface have long been proved to contain quantitative information about ocean surface slope statistics (e.g. Barber, 1949; Cox and Munk, 1956), to help infer directional spectra of surface waves (Stilwell, 1969; Stilwell and Pilon, 1974). Today, with the

significant cost reduction and improvement of both instruments and drones, the photograph techniques may become more widely used to observe and monitor surface waves at regional or coastal scales.

Since almost two centuries (Spooner, 1822), it has been understood that the shape of the sunglint on the sea surface contains information on the statistical properties of wave slopes. Airborne and satellite sunglint images at medium ($\sim$ 1 km) resolution have then been used to precisely estimate sea surface slope statistical properties (Cox and Munk, 1956; Breon and Henriot, 2006), and modulations by various dynamical ocean processes like currents and fronts, internal waves, or surface slicks (Barber, 1954; Apel et al., 1975; Hennings et al., 1994; Kudryavtsev et al., 2012; Kudryavtsev et al., 2012; Rascle et al., 2016, 2017). At higher ($\sim 1 - 10$ m) resolution, glitter modulations are more directly connected to the wavy surface. Indeed, wave contrasts on the image result from the modulation of sun reflected radiation by individual tilting wave slopes, and those can be used to estimate the wave directional elevation spectrum (Stilwell and Pilon, 1974; Monaldo and Kasevich, 1981).

To derive wave elevations from these brightness variations, a transfer function must thus be determined. Using airborne photographs, this task is eased,

as the overall sunglitter shape can be captured, to help directly infer a linear transfer function (Bolshakov et al., 1988). Recently, Yurovskaya et al. (2018) demonstrated the technical implementation to retrieve wind wave spectrum from sunglitter photographs taken from a drone. Adapted to a satellite configuration, such a method was also successfully applied (Kudryavtsev et al., 2017a,b) to reconstruct the spectrum of long (energy containing) waves from satellite sunglitter images, taking advantage of the high resolution and specific viewing geometry of the radiometers on-board the satellite Sentinel-2.

In this paper, we further dwell on this capability of airborne sunglitter imagery to capture the overall glitter pattern. As mentioned above, this property provides direct means to determine a linear transfer function. Our motivation is then to further assess how robust is our proposed methodology to efficiently provide quantitative estimates of the directional wave spectrum, including energy containing waves and also short waves. The development is specific to airborne measurements and applied to data collected over a coastal area in the northern Gulf of Mexico.

The paper structure is as follows. The experiment is described in Section 2; theory and spectrum reconstruction algorithm are presented in Section 3; method implementation and validation are given in Section 4; the

results of the study of wave development and transformation with fetch are presented in Section 5, and finally, the discussion of method applicability and some recommendations on experimental setup are suggested in Section 6.

2. Experiment and Data

The airborne sunglitter images were obtained on Jan. and Feb. 2016 during the Lagrangian Submesoscale Experiment (LASER), where a large number (~ 1000) of surface drifters were deployed to study surface dispersion within the Gulf of Mexico (D'Asaro et al., 2018; Rascle et al., 2017), close to the site of the Deep Horizon oil platform accident in 2010 (Fig. 1, a). The images were acquired from airplane (a Partenavia P.68) flying at altitudes up to 3000 m.

The visible light intensity was measured by two panchromatic cameras (JAI BM-500GE) equipped with a 5 mm focal length low distortion lens to ensure a large field of view. The cameras setup is sketched in Figure 1, b. To capture the sunglint, the two cameras were arranged symmetrically about the airplane nadir with a pitch of $\pm 35^\circ$ for the forward/aftward cameras. The camera aperture angles are $80^\circ \times 70^\circ$ along-track and across-track, respectively, with 2456×2058 pixels in the respective directions. For a flight

altitude of 1000 m, this leads to a ground resolution from 0.5 m to 6 m. The cameras acquired images at 2 Hz. The images were geolocated using an internal motion unit Applanix POS AV V610.

We selected cases corresponding to measurements made during flights with trajectories close to National Data Buoy Center (NDBC) buoy locations, to benefit from synchronous wind and wave ancillary data. A step by step algorithm is provided for images obtained close to NDBC 42012 in developed wind sea conditions on 11-Feb-2016 (green star on Fig. 1, a). Further we analyze the wave evolution on 23-Jan-2016, when sunglitter images were acquired (in cloudless regions) at different distances from the shore along the plane tracks shown in Fig. 1, a.

3. Theoretical Background

Based on the classical model of the sea surface brightness formation in the visible range (Cox and Munk, 1956), the intensity in each pixel of sunglitter image is proportional to the sun reflected radiance, or the energy brightness of the surface (the spectral energy flux per unit area per unit solid angle):

$$N = \frac{\rho E_s}{4 \cos\theta \cos^4\beta} P(Z_1, Z_2), \tag{1}$$

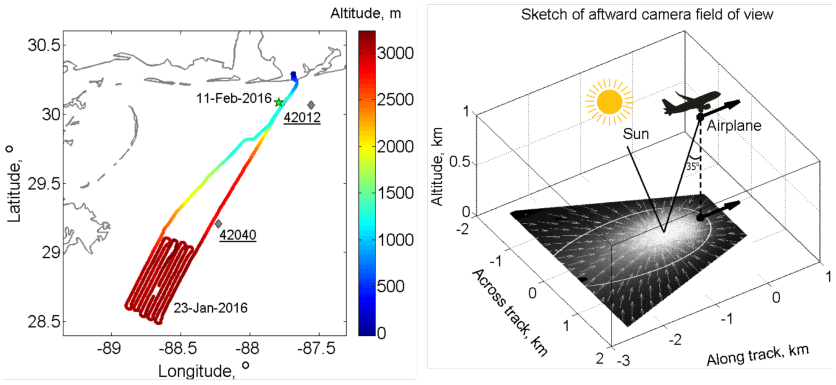

Figure 1: (a) The observation area with NDBC buoy locations (gray diamonds). Green star shows location of the analysis on 11-Feb-2016 (section 4), colors are the tracks of the 23-Jan-2016 flight (section 5). (b) Sketch of the field of view of the afterward camera, for a flight altitude of 1000 m. Here we show the special case of the sun exactly at the rear of the airplane when the specular sun spot is at the center of the camera field of view. The ellipse is the contour $Z_n^2 = s^2$ (see the notifications below). The white arrows show the orientations of the transfer function gradient, G_{zi}.

where P is the probability density of two slope components, Z_1, Z_2, satisfying the conditions of specular reflection:

$$Z_1 = -\frac{\sin\theta_s \cos\phi_s + \sin\theta \cos\phi_\nu}{\cos\theta_s + \cos\theta}$$
$$Z_2 = -\frac{\sin\theta_s \sin\phi_s + \sin\theta \sin\phi_\nu}{\cos\theta_s + \cos\theta}, \tag{2}$$

θ and θ_s are zenith angles for the camera and the sun, respectively, ϕ_ν and ϕ_s are corresponding azimuth angles, ρ is the Fresnel reflection coefficient,

E_s is the solar radiance, $\tan\beta = \sqrt{Z_1^2 + Z_2^2}$.

Local modulations of $B = N\cos\theta/\rho$, or equivalently, of P, can arise for two reasons: variations of the slope statistics mostly governed by changes of mean square slope (MSS) due to different upper ocean processes (fronts, internal waves, surface slicks, etc), or the tilting of the ocean surface while a long wave is propagating. The latter can also lead to a short wave (and thus, MSS) modulation along the wave profile. As demonstrated by Bolshakov et al. (1988) and Kudryavtsev et al. (2017a), one can ignore these MSS modulations in the vicinity of brightness contrast inversion zone, i.e. $0.5 < Z_n^2/s^2 < 2$, where $Z_n^2 = Z_1^2 + Z_2^2$, and s^2 is the surface MSS to the first order estimated from the assumption of Gaussian brightness and slope distribution as $s^2 = -2\overline{Z_n} \cdot \overline{B}/(\partial B/\partial Z_n)$. The brightness variation due to the long wave propagation then writes:

$$\tilde{B} = B(Z_1 + \zeta_1, Z_2 + \zeta_2) - B(Z_1, Z_2) = \frac{\partial B}{\partial Z_i}\zeta_i \equiv G_{zi}\zeta_i, \tag{3}$$

where $\zeta_{1,2}$ are the components of tilting wave slope. G_{zi} is the transfer function, relating brightness and slope variations. This transfer function is then determined as the brightness gradient in specular slope space and can be obtained through the observed brightness gradients:

$$G_{z1} = (G_2 Z_{2,1} - G_1 Z_{2,2})/\Delta$$

$$G_{z2} = (G_1 Z_{1,2} - G_2 Z_{1,1})/\Delta, \tag{4}$$

where $G_i = \partial B/\partial x_i$, $Z_{i,j} = \partial Z_i/\partial x_j$, $\Delta = Z_{1,2}Z_{2,1} - Z_{1,1}Z_{2,2}$.

Eq. (1) relates the mean brightness to surface slope statistics, as in the work of Cox and Munk (1954). On the contrary, (3) and (4) relate local brightness variations to local slope variations. In the Fourier space the surface slope ζ_j and the surface elevation ξ are linked by: $\hat{\zeta}_j = ik_j\hat{\xi}$, where i stands for imaginary unit. Thus, equation (3) in the Fourier space reads: $\hat{\tilde{B}} = ik_j G_{zj}\hat{\xi}$, and the relationship between the surface elevations and brightness spectra writes:

$$S_\xi(\mathbf{k}) = S_B(\mathbf{k})/(G_{zi}k_i)^2. \tag{5}$$

The linear combination of wave vector components in the denominator of (5) vanishes in a direction perpendicular to the gradient direction. Close to this direction, the spectrum cannot be simply retrieved. For Sentinel-2 multi-spectral satellite imagery, recently reported by Kudryavtsev et al.

(2017a,b), this limitation was mitigated by interpolating the spectrum in a narrow wavenumber sector encompassing the singularity. A clear advantage of airborne photography (compared with satelllite scanners) is that it captures the two-dimensional field of view of the sunglitter brightness. Therefore, relation like (5) can be obtained in different parts of the sunglitter, corresponding to directions for which the brightness gradients are different. As suggested by Bolshakov et al. (1988) and also Lupyan (1988), the singularity can be eliminated, by using several image fragments with different gradients G_{zi}^n, but statistically identical wave spectrum, $S_\xi^n(\mathbf{k}) = S_\xi(\mathbf{k})$. As sketched in Fig. 1, b, where the typical distribution of G_{zi}^n orientations is shown, the vectors converge towards the sunglitter center, changing their direction from 0° to 360° around it. Brightness spectra taken from fragments with different vector orientations can then be averaged, to obtain the elevation spectrum without any singularity:

$$S_\xi(\mathbf{k}) = \sum_{n=1}^{N} S_B^n(\mathbf{k}) / \sum_{n=1}^{N} (G_{zi}^n k_i)^2. \tag{6}$$

As described, the considered methodology is self-consistent, solely based on the transfer function estimation from the observed shape of solar glint. For airborne photography, the following steps must then be taken:

- gradients G_i, $Z_{i,j}$ are determined from the smoothed sunglitter pattern and known geometrical parameters;
- a transfer function, G_{zi}, is calculated using (4);
- several image fragments are selected in different image parts, still in the vicinity of contrast inversion zone, and their brightness spectra are calculated;
- the absolute directional wave elevation spectrum is derived from the sum of brightness spectra and transfer function field, using expression (6);
- 180-degree wave direction ambiguity can be removed using cross-correlation analysis of two consequent images.

A detailed example of airborne sunglitter image processing is given below.

4. Method Implementation

4.1. Image preprocessing

On 11-Feb-2016, a snapshot of the sea surface (Fig. 2, a) was extracted close to the location of the NDBC buoy number 42012 (Fig. 1, a). The wind

was about 9 m s^{-1} blowing from South-West, and peak waves of about 40 m wavelength were propagating from the same direction.

The above procedure must be applied to a brightness field predominantly formed by the sunlight reflections from the sea surface. Besides the image projection onto the sea surface plane (Fig. 2, b), a preparatory step is to consider an intensity correction to possibly account for extraneous factors hampering the image brightness. We neglect any vignetting effect and consider the image intensity proportional to the energy surface brightness, N. First, the sky reflection and scattered radiation can contribute to the image brightness. Cox and Munk (1956) report corresponding dependencies on incidence angle by considering intensities from regions far outside the glitter. A similar procedure is to use the darkest column of the photograph (the right one in the example on Fig. 2, a). Given the viewing geometry and neglecting the sunglitter contribution within this darkest line, the incidence angle dependency of the background radiance can be estimated. A corresponding polynomial approximation, Fig. 2, c, is then assumed to extend over the whole 2D image, and further subtracted. Nevertheless, in all considered examples, we do not use parts of the images with $\theta > 50°$, areas over which the impact of scattered radiation rapidly grows (Cox and Munk, 1956), and the

assumption (3) loses its validity.

According to (1), the detrended field, $N - N_{back}$ (not shown), should be multiplied by $\cos\theta/\rho$, shown in Fig. 2, d. Values of $\cos\theta/\rho$ differ up to 4-5 times on the opposite image borders with incidence angles 25^o and $60°$. This operation suppresses the brightness of the distant zone and shifts the sunglitter center towards the edge corresponding to the lowest incidence angle (compare Fig. 2, b and Fig. 2, e). The mean brightness field, B_0 (Fig. 2, f), is then derived by smoothing $B = (N - N_{back})\cos\theta/\rho$ using a moving average filter, with a window size depending on the image resolution (about several lengths of dominant wave). All the algorithm steps then apply to the brightness variation field, $B - B_0$.

4.2. Spectrum validation

A fragment of the brightness variation field is shown Fig. 3, a. Fragments are taken between the two ellipses indicating the zone $0.5 < Z_n^2/s^2 < 2$, and above the line $\theta = 50°$.

Fig. 3, b displays the sum of directional brightness spectra. As expected, the resulting transfer function, $\sum(G_{zi}^n k_i)^2$ (Fig. 3, c), does not vanish in any particular direction, but tends to zero in the wavenumber plane center. This may enhance noise level and errors at the lowest wavenumbers. After

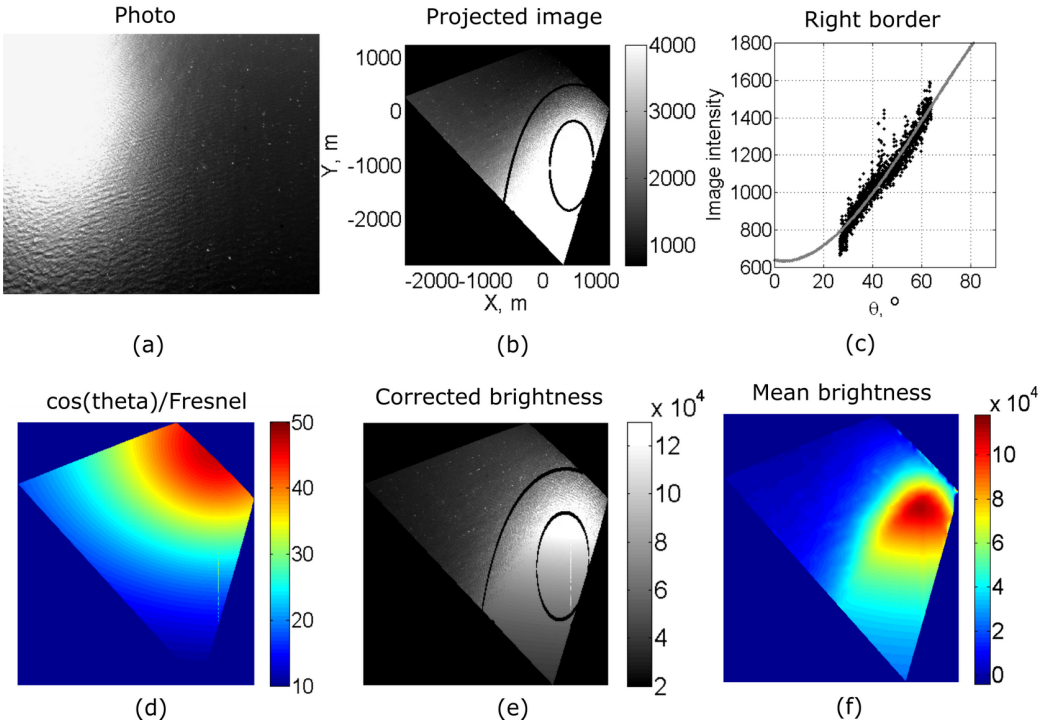

Figure 2: (a) An airborne snapshot of a sea surface; (b) image projected on the sea surface plane (x-label is to the East, y-label is to the North, two ellipses determine the zone $0.5 < Z_n^2/s^2 < 2$); (c) pixel intensities for the left column of a photo (dots) and their polynomial approximation indicating the background radiation; (d) $\cos\theta/\rho$ field; (e) $B = (N - N_{back})\cos\theta/\rho$ field; (f) mean brightness field, B_0

application of the transfer function, Fig. 3, d, both brightness and wave elevation spectra possess a distinct spectral peak, visually corresponding to the waves observed on the fragment, Fig. 3, a, but the angular distribution of the elevation spectrum is apparently broader, possibly revealing waves moving closer to zonal (eastward or westward) directions.

The comparison with the nearby NDBC buoy wavenumber directional spectrum (Fig. 3, d), calculated with the use of the maximum entropy method (Lygre and Krogstad, 1986) and linear dispersion relation for gravity waves, gives a satisfactory agreement of 2D energy distribution. Notice that in contrast to NDBC data that provides a "true" directional spectrum, the spectrum retrieved from the image is folded ($S(\phi) = S(\phi) + S(\phi + 180°)$) having a 180-degree ambiguity in wave direction.

Omnidirectional spectra are compared in Fig. 3, f, and give an excellent agreement of peak position and its energy level. Energy underestimation of retrieved spectrum at wavenumbers $k > 0.3$ rad/m can be explained by the actual (not interpolated) image resolution and smoothing of features smaller than 10 m. The noise level at $k < 0.1$ rad/m depends on the B_0 calculation (the smaller the filter window size, the lower the spectrum), and is also controled by the singularity of a transfer function around $k = 0$ rad/m.

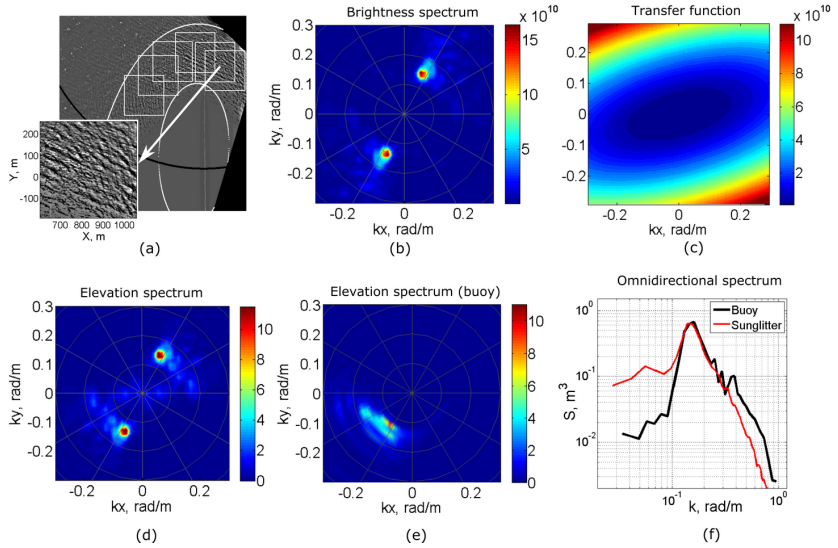

Figure 3: (a) Square fragments (450 m size) of brightness variation field, $(B - B_0)$, taken for spectrum retrieval. Two ellipses determine the zone $0.5 < Z_n^2/s^2 < 2$, black line is $\theta = 50°$; (b) The sum of brightness spectra; (c) the transfer function, $\sum_{n=1}^{N}(G_{zi}^n k_i)^2$; (d) retrieved from (6) elevation spectrum; (e) NDBC buoy data directional spectrum (42012); (f) Omnidirectional spectra comparison.

Energy distribution of waves in a range 20 m - 60 m is reliably reproduced.

4.3. Wave direction ambiguity

In our cases, the camera acquired images every 0.5 s. Consecutive snapshots can then be analyzed to remove the wave propagation directional ambiguity (Fig. 3, d), as already demonstrated for satellite measurements (Kudryavtsev et al., 2017a; De Michele et al., 2012). Two images of the same square region of the sea surface taken with a Δt =0.5 s time difference are shown on Fig. 4, a-b. Their spectral coherence, $< \hat{I}_2 \hat{I}_1^* >^2 /(< \hat{I}_1 \hat{I}_1^* >< $

$\hat{I}_2\hat{I}_2^{\,*} >$), hat means the Fourier transform, a star is complex conjugation, and phase, $\arg(< \hat{I}_2\hat{I}_1^{\,*} >)$, are given in Fig. 4, b-c. The coherence level is high, up to 1, in the direction where the waves are observed. The phase spectrum is a-priory asymmetric, and the positive phase shift corresponds to the direction "from" in a case when I_1 is taken earlier than I_2. Thus, the wave system is moving from South-West, to agree with the NDBC directional spectrum (Fig. 3, b).

Airborne image time series can further be used to estimate ocean surface currents from the dispersion of the detected gravity waves (e.g. Dugan and Piotrowski (2003)). Taking a transect in the phase spectrum, $\Delta\Phi$, along a direction corresponding to maximum coherency, marked with a dashed line in Fig. 4, the dispersion can be evaluated for the relative projection of the phase velocity: $c(k) = \frac{\Delta\Phi/\Delta t}{k}$. As obtained, Fig. 4, e, experimentally derived points lie very close to the standard prediction, $c = \sqrt{g/k}$, even at large wavenumbers for which the elevation spectral analysis is less reliable. This indicates the absence of surface current, or at least its component along the chosen direction, in the region of observation.

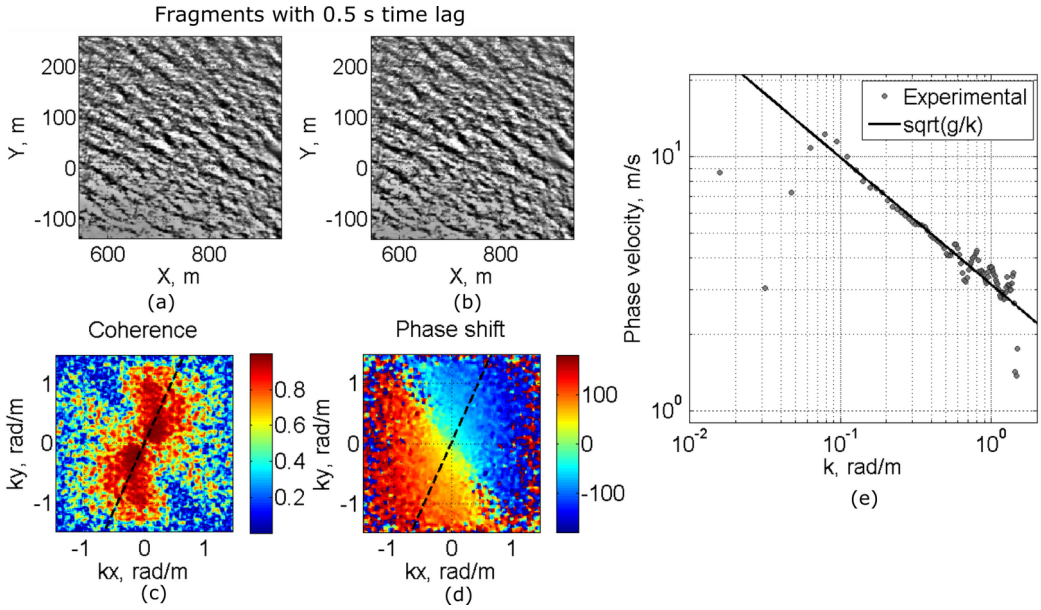

Figure 4: (a)-(b) Snapshots of the same location taken with 0.5 s time shift; (c) coherence of two brightness fields; (d) phase shift; wave direction (from) corresponds to positive values of a phase shift; (e) dispersion relation calculated from a phase shift along the line of coherence maximum (dashed lines in (c) and (d) plots).

5. A Case Study: Spectrum Evolution with Fetch

On 23-Jan-2016, an experiment to study wave transformation at varying distance from the shore was conducted. The airplane moves seawards across the NDBC 42012 and 42040 locations (Fig. 1, a, and Fig. 5). The flight started at 19:20 UTC in clear sky conditions, but at 19:31 the plane entered a cloudy zone with gleam areas too small to estimate the wave spectrum. Yet, two images at 19:50 could be exploited. On the way back, at 23:00, camera pitch and sun elevation angle didn't satisfy the condition $Z_n^2/s^2 < 2$ and clouds were still hindering the glitter. As a result, only one image fragment from the glint periphery could be used, with relatively low reliability.

The wind speed and direction (in nautical system) around the time of acquisition are plotted in Fig. 6. Wind was blowing from the North-West, slightly rotating clockwise and calming down from 12 m s^{-1} to 10 m s^{-1}, accordingly to NDBC 42040 data. The slow clockwise wind rotation took place during the previous two days, starting to blow from South, then West, before finally subsiding to 3 m s^{-1} from North on 24-Jan.

The two-dimensional slope spectra (Sk^2) from the buoys are shown in Fig. 6. The slope spectra, reconstructed from the airplane images are shown in Fig. 7, for the points marked by red squares on the map of Fig. 5. Many

different wave systems co-exist in the area (see sketch Fig. 5).

First, there is a long ($k \sim 0.05$ rad m^{-1}) swell from West-South-West, probably originating from West of the Mississipi delta and entering the area from the South-West. This swell is well observed at buoy 42040 (Fig. 6, bottom right) and on the airplane spectra at 22:50 (Fig. 7). It is not properly resolved by the small image fragments used around buoy 42012 and is weakly seen on the buoy data (Fig. 6, bottom left) as the Southern swell.

Also, there is the wind sea at short wavenumbers ($k > 0.1$ rad m^{-1}). The peak of the wind sea is slightly more from the North than the wind direction (marked by a white dashed line in Fig. 6 and Fig. 7), both on buoy data and on the airplane spectra. Third, there is a series of spectral peaks from West to North-West (see before 19:31 on Fig. 7, see also buoy data on Fig. 6). Those peaks are typical of slanting fetch conditions (Ardhuin et al., 2007, e.g.), where the wind sea separates between subsystems, the high-frequency remaining downwind whereas waves at relatively lower frequency develop and propagate in the slanting fetch direction (along-shore). Very close to the shore (before 19:25 on Fig. 7), those slanting short waves even dominate the wind sea spectrum.

From the analyzed spectra, the main tendency is a gradual peak shift-

ing towards lower wavenumbers and a corresponding energy growth with the fetch distance. These effects are better identified in omnidirectional spectrum evolution, Fig. 8. The figure presents angle-integrated surface elevation spectrum (red) together with buoy-derived spectra at 19:00 (t1, black) and 20:00 (t2, gray) for NDBC 42012, and at 21:00 (t1) and 23:00 (t2) for NDBC 42040. To help the interpretation, empirical model spectra, as suggested by Donelan et al. (1985) and Babanin and Soloviev (1998), are displayed, for different fetches (given in figure titles). Fetches are calculated as the distance to the line passing through alongshore islands (bold green on Fig. 5) in the direction of the wind taken from the nearest buoy. They are further corrected to account for the direction of the spectral peak mostly deviating from NDBC wind direction. At small fetches (below 5-10 km), the spectrum is rather variable in energy level and peak position, also probably due to the changing bottom topography and consequent refraction effects. The wind wave peak is hardly distinguished and only starts to be clearly obtained at fetch about 10 km. At 19:25:31, the fetch value is close to the one captured at NDBC 42012 location (see Fig. 5). The respective spectra are then found very close (compare black and red curves in Fig. 8). The evolution then continues and closely follows Donelan et al. (1985) and Babanin and Soloviev (1998) pre-

dictions. Despite the low reliability for the sunglitter-derived spectrum at 22:50 (the last subplot), a good agreement is found with both model and buoy data taken at approximately the same fetch.

To generalize the wind sea peak transformation, we present (Fig. 9, a) the dependency of dimensionless peak frequency, $f_p u_{10}/g$, and dimensionless energy, Eg^2/u_{10}^4, estimated as the spectrum integral around the wind wave peak and shorter waves, on dimensionless wave fetch, Lg/u_{10}^2. Comparison is made with other data collected by Babanin and Soloviev (1998). As obtained, results are consistent with the cited approximations, except for the wave energy at the near-shore points. For these cases, the wind peak wavelength is not far from the camera resolution.

The present data, unfortunately, cannot trace any pronounced tendency for the angular distribution evolution. This is due to the presence of several swell peaks much stronger than the wind ones, and inaccurate data at large fetches, where the wind peak dominates. Yet, the average angular distribution around the peak wavenumber (Fig. 9, b) does not contradict the dependency, $S(k_p) = 0.5\beta/\cosh^2(\beta\phi)$, $\beta = 2.28$, reported by Donelan et al. (1985), confirming that multi-modal spectrum structure provides some broadening at the angles far from $\phi = 0$ (peak position).

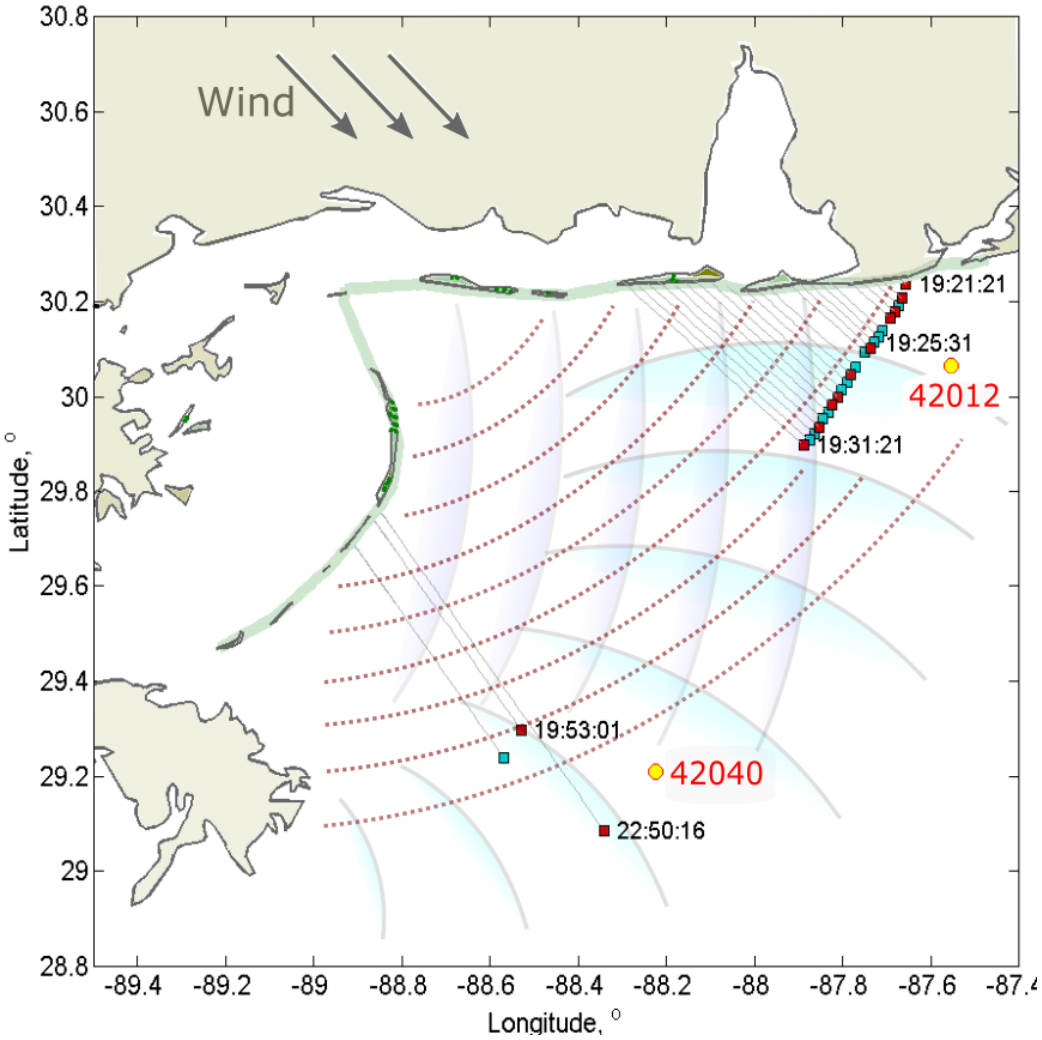

Figure 5: Locations of the images acquired on 23-Jan-2016 near NDBC buoys 42012 and 42040, and schematic wave systems orientations.

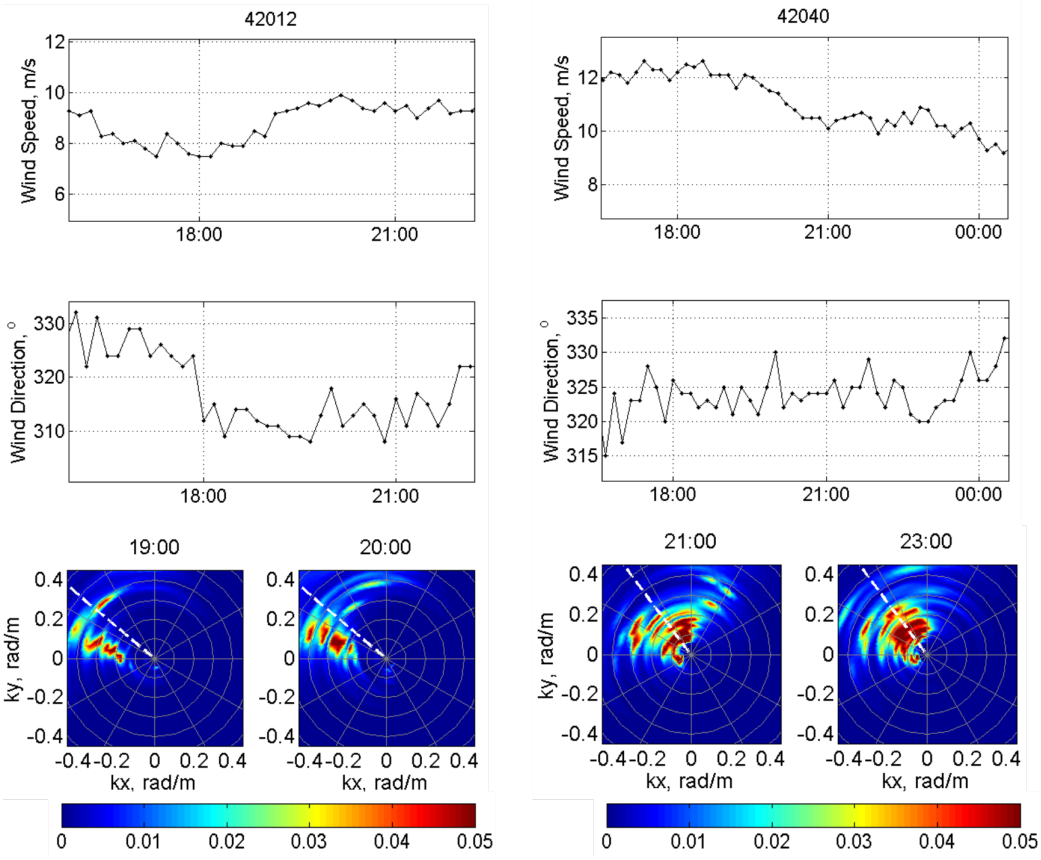

Figure 6: Windspeed, wind direction and directional slope spectra from NDBC 42012 and 42040 buoys around the time of airplane flight. Wind and wave directions are ‘’from” in nautical system.

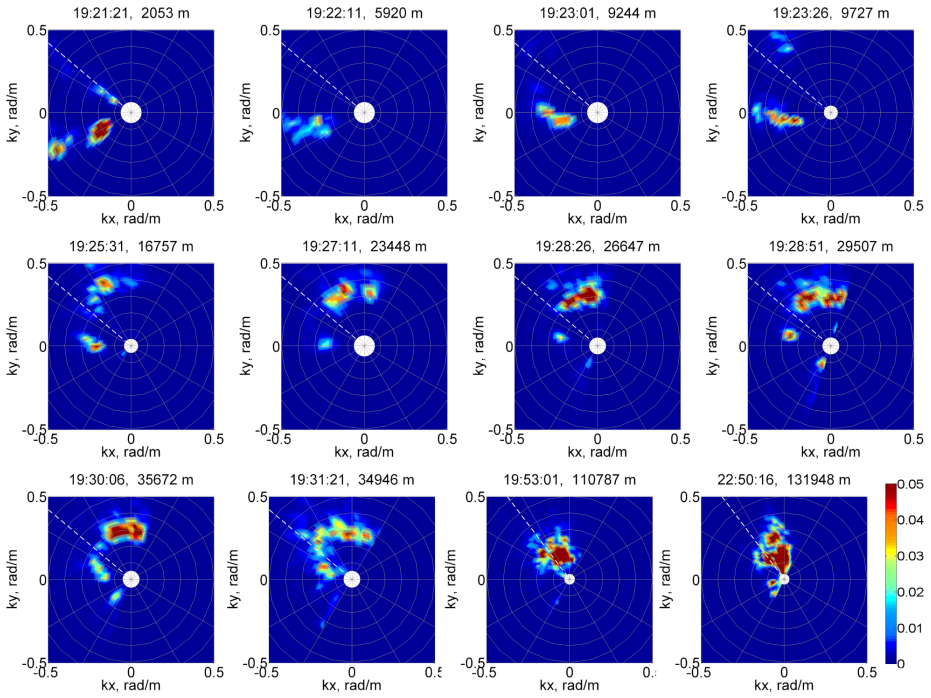

Figure 7: Directional slope spectra at the points marked by red squares on fig 5. White line is the wind direction from buoy data (trigonometrical system). Spectrum develops in presence of swell from West. Wind wave peak grows and shifts towards low wavenumbers, slightly deviates from NDBC wind direction (actually the wind also changed its direction).

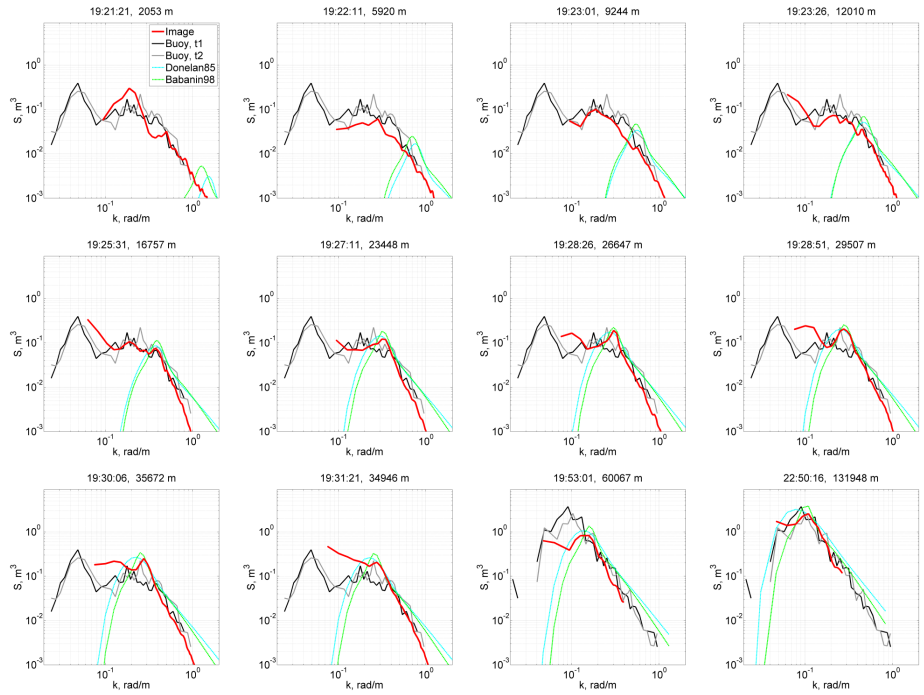

Figure 8: Omnidirectional spectra at the points marked by red squares on fig 5. Wind peak grows and shifts towards lower wavenumbers in consistence with Donelan et al. (1985) and Babanin and Soloviev (1998) spectra. Blue (Babanin and Soloviev, 1998) and green (Donelan et al., 1985) curves are given for the wind speed taken from the nearest buoy (42012 or 42040) and the fetch is corrected accounting for the spectrum wind wave peak direction estimated from Fig. 7.

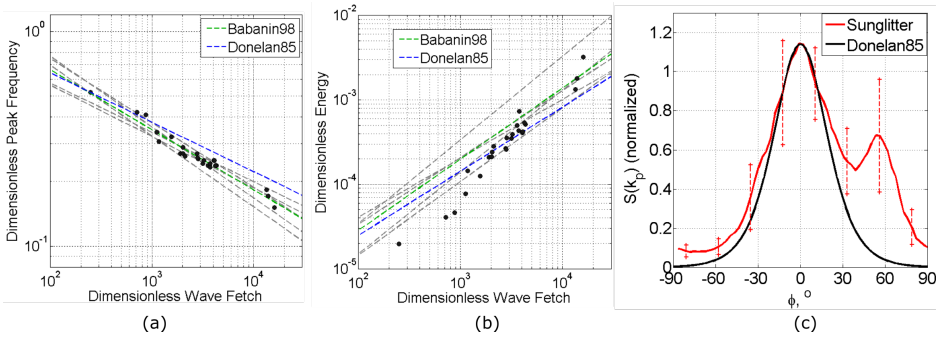

Figure 9: (a) Dimensionless peak frequency vs. dimensionless fetch. Black circles – experimental points (all retrieved spectra), dashed lines – approximations from other authors (Davidan, 1980; Babanin and Soloviev, 1998; Donelan et al., 1985; Kahma, 1981; Dobson et al., 1989; Wen et al., 1989; Ewans and C. Kibblewhite, 1990) for the wind speed 9 m s^{-1}; (b) Dimensionless peak frequency vs. windsea demensionless variance with the same notations; (c) angular function suggested by Donelan et al. (1985) and ensemble average wave energy distribution around the peak wavenumber ($0.75k_p < k < 1.25k_p$); the length of vertical lines is equal to standard deviation.

6. Method Applicability and Constraints

As demonstrated, the proposed spectral reconstruction robustly applies when several requirements are satisfied.

The photograph should contain a part of sunglitter ellipse, $Z_n^2 = s^2$, within the camera incidence angle range $\theta < 50^o$. The area must be large enough to provide sufficient angle diversity between the transfer function vectors that are about normal to the ellipse. This ensures to properly eliminate the singularity of the transfer function. The brightness of the observed area should not be saturated. A saturation shortens the range of slope values. Clouds are also to be avoided. Cloudiness, or other inhomogeneities, impact

the estimation of the mean brightness characteristics.

The question of the impact of wave breaking is still open. Breakers can appear on the image as bright spots, to possibly distort the retrieved slope/elevation distribution. Under high-wind conditions, individual breakers shall be excluded, and individual breaking crests possibly interpolated.

Coming back to the part of the sunglint where the spectrum can be derived, i.e. $0.5 < Z_n^2/s^2 < 2$ and $\theta < 50^o$, a simplified one-dimensional analysis leads to a necessary condition for the camera zenith angle: $\beta_1 < |\theta - \theta_s| < \beta_2$, where $\beta_1 = 2 \arctan \sqrt{0.5 s^2}$, $\beta_2 = 2 \arctan \sqrt{2 s^2}$ with $s^2 = 0.003 + 0.00512 U_{10}$ (Cox and Munk, 1956). Close to the camera nadir direction (Fig. 1), the distance between the two curves represents the longest wavelength being detected,

$$d_{long} = H \left[\tan(\theta_s - \beta_1) - \tan(\theta_s - \beta_2) \right], \tag{7}$$

where H is the plane altitude.

The shortest wavelength being detected depends on the camera technical parameters, the camera view angle, γ, and the image pixel size, N_p. The 1D spatial resolution, the Nyquist wavelength, in and around the vicinity of the

lens optical line-of sight axis, reads:

$$d_{short} = \frac{4H \tan(\gamma/2)}{N_p \cos\theta}, \tag{8}$$

for an altitude H and zenith angle θ.

Values of d_{long} for different sun zenith angles and different wind speeds, and of d_{short} for $N_p = 1000$, different camera view angles and two boundary camera zenith angles θ (nadir and 50^o), are presented in Fig 10, a, b, as functions of camera altitude. It summarizes the range of wave scales that can potentially be resolved from a sunglitter photograph.

As shown, Fig. 3, f, and Fig 8, measurements from an altitude $H \simeq 1 - 1.5$ km, with $N_p \simeq 2000$, $\theta_s \simeq 45^o$, $\gamma = 80^o$, provide a wave spectrum defined in a range between 3-5 m to 200-300 m as predicted by fig. 10, but the effective reliable range is much more reduced: from 10-20 m to 50-60 m. At high wavenumbers, the estimate (8) is certainly too optimistic, compared to the real optical resolution possible to achieve. Indeed, the estimate stands for the case of perfect focusing lens, and total absence of any blurring effects from airplane movements and/or camera jitters. In the present experiment, these ideal conditions are not realized, leading to an effective 2-3

pixel smoothing of the image brightness.

For the lower wavenumber limit, a reliable spectrum estimation shall require a window size to encompass at least three to five wavelengths of dominant surface waves, especially considering the singularity of the transfer function around $k = 0$. Thus, the practical maximum wavelength is at least three times shorter than d_{long}.

In addition, as recently discussed by Yurovsky et al. (2018) to analyze radar measurements, low-frequency parts of derived spectra may be corrupted by a "non-linear energy leak" process, from the spectral peak towards lower frequencies. This effect results from the non-linearity of the modulation transfer function (MTF). Accordingly to their Fig. 11, an artificial amplification of the spectrum in the low-frequency range, at frequencies lower than the spectral peak frequency, is solely governed by the MTF magnitude. In terms of sunglitter imagery, the MTF, which quantifies the short wave modulations by the underlying longer waves, is equal to: $M_i = 1/B_0 \partial B/\partial Z_i \approx -2Z_j/s^2$ (see eq. 9 of Kudryavtsev et al. (2017a)). For winds around 5-7 m/s, $s^2 \approx 0.04$, and observing conditions $0.5 < Z_n^2/s^2 < 2$, the MTF range becomes $M = 7 - 14$. Refering to Fig.11 by Yurovsky et al. (2018), we may postulate that such rather large MTF values could artificially enhance the

low-frequency spectral level, $\sim (0.1 - 0.3)S(k_p)$ (to the left of the spectral peak), increasing up to $(0.7 - 1.0)S(k_p)$ with decreasing wavenumber. These estimates agree well with reported spectral levels at low-wavenumbers, Fig. 3, f, and Fig. 8. As understood, this "non-linear energy leak" process relates to the impact of spectral peak modulations on the retrieved spectral levels in adjacent low-frequency intervals. Correspondingly, if the spectral peak wavelength is larger than d_{long}, the retrieved spectrum shall be valid over the full wavenumber range, as e.g. in the cases on upper subplots of Fig. 8.

Thus, despite some additional constraints, nominal estimates given in Fig. 10 are useful to guide experiments and the analysis for different situations. With growing airborne and photo/video technique capabilities, the method validity range shall likely rapidly improve, mostly thanks to increased image resolution and measurements taken at higher altitudes.

As a final remark, we note that, to retrieve spatio-temporal wave characteristics, the requirement of a perfect sunglint is less strict. Indeed, those characteristics can be derived directly from the surface brightness field and do not need the surface elevation spectrum. The previous stringent requirements apply to robustly retrieve the wave elevation spectrum from a sunglint photograph. Other spatio-temporal wave characteristics, such as the deter-

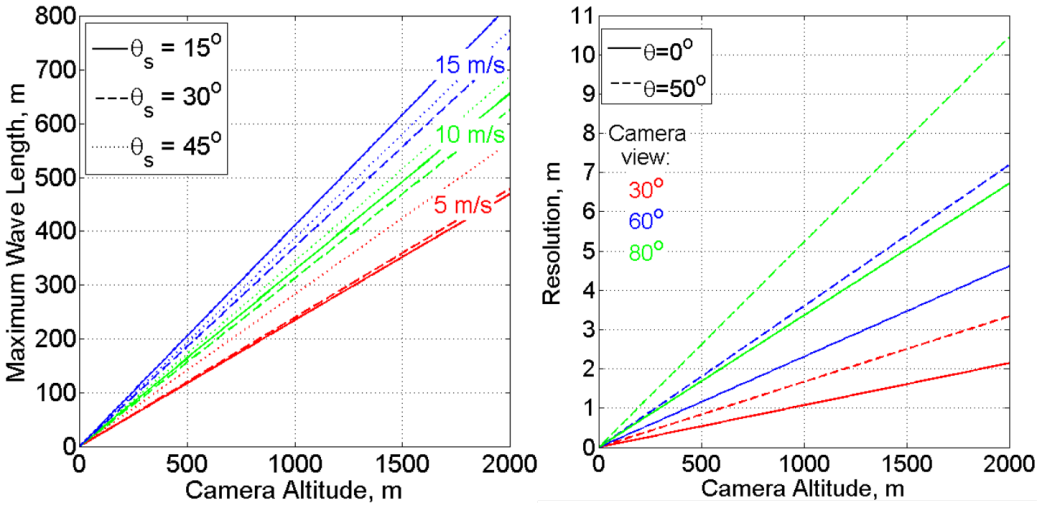

Figure 10: Left: the longest waves which can be observed within the useful part of the sunglint ($0.5 < Z_n^2/s^2 < 2$), as function of the camera altitude H. Three different sun zenith angles ($\theta_s = 15, 30, 45^o$) and three different wind speeds ($5, 10, 15$ m s^{-1}) are used for the calculations. Right: surface resolution as a function of camera altitude for the image size $N_p = 1000$ pixels, different camera view angles and two camera zenith angles ($\theta = 0^o$ and $\theta = 50^o$)

mination of a surface current-induced Doppler shift in the dispersion relation, merely needs to follow individual wave crests. As such, it can be applied further away from the sunglint, or even using the sky glint. Yet, a perfect geolocation might be required to accurately estimate wavelengths and shifts, and it is therefore recommended to work with images at small incidence angles.

7. Conclusion

In this paper, the efficient implementation of a two-dimensional wave spectrum reconstruction algorithm has been demonstrated and applied to analyze airborne sunglitter photographs acquired during an experiment in the Gulf of Mexico. A linear transfer function to relate the image brightness variations to surface elevations is simply deduced from the shape of the glint. The singularity in wavenumber space, inherent to this approach, is eliminated by using several image fragments corresponding to different directions of the transfer function gradient. This was earlier suggested by Bolshakov et al. (1988) and Lupyan (1988), and was also applied to drone measurements (Yurovskaya et al., 2018) and satellite observations by Kudryavtsev et al. (2017a). Following this methodology, the absolute wavenumber elevation spectrum does not require any additional assumption or ancillary information about the sky brightness, wind or wave energy.

As also demonstrated, a cross-correlation analysis between consecutive photographs, taken with a small time lag (0.5 s), resolves the 180-degree ambiguity to provide the wave direction. Further, using a transect in the resulting phase spectrum gives an estimate of the wave dispersion along the propagation direction. As tested, comparisons between retrieved spectra and

nearby NDBC buoy estimates are in good agreement, for both the spectral level and energy angular distribution.

A case study corresponding to the wave spectral evolution with increasing distance from shore in slanting-fetch conditions has then been considered, and further provide convincing evidence of the applicability and validity of the proposed method. Indeed, energy level and peak position transformation agree well with established approximations and laws of the wind-sea development, and quantitatively compare with previous experimental data and model predictions (Donelan et al., 1985; Babanin and Soloviev, 1998; Ardhuin et al., 2007).

In the context of today's rapidly growing technologies and the development of relatively simple remote controlled measurements from drones, the straightforward algorithm described here will provide efficient means to renew and enhance the interest of aerial photographs of ocean sunglint patterns. Combined with the satellite sunglitter data processing (Kudryavtsev et al., 2017a), such measurements could provide wave characteristics at shorter scales, to infer comprehensive quantitative information about surface wave properties and related rapid transformations over coastal areas.

Acknowledgment

We are grateful to Fabrice Ardhuin for the help in NDBC data processing and to Vladimir Dulov for the fruitful discussions. The work was supported by Russian Science Foundation via grant 17-77-30019. The support of FASO of Russia under the State Assignment (No. 0827-2018-0003) and ESA SARONG project are also acknowledged.

Appendix A. Symbol Definitions

Symbol	Definition
β	Tilt angle for sunlight specular reflection
γ	Camera view angle
ζ_1, ζ_2	Surface slope components
θ	Camera zenith angle
θ_s	Sun zenith angle
ξ	Surface elevation
ρ	Fresnel reflection coefficient
Φ	Wave phase spectrum
ϕ	Wave vector angle
ϕ_ν	Camera azimuth angle
ϕ_s	Sun azimuth angle

B	Modified image brightness, $\sim N\cos\theta/\rho$
B_0	Mean (smoothed) image brightness
c	Wave phase velocity
E	Wave peak energy
Es	Solar radiance
f_p	Spectrum peak frequency
G_i	Brightness gradient components, $\partial B/\partial x_i$
G_{zi}	Transfer function components, $\partial B/\partial Z_i$
g	Earth gravity, 9.8 ms^{-1}
H	Camera altitude
I_i	Image brightness fragments
k	Wavenumber vector
k_p	Spectrum peak wavenumber
L	Wave fetch
M	Modulation transfer function
N	Reflected radiance
N_p	Image pixel size
N_{back}	Background radiance (sky reflected and scattered)
P	Probability density of slope components
S_ξ	Surface elevation spectrum
S_B	Surface brightness spectrum
s^2	Surface mean square slope (MSS)
U_{10}	Wind speed at 10 m
Z_1, Z_2	Surface slope components, providing specular reflection
Z_n	Specular slope absolute value, $\sqrt{Z_1^2 + Z_2^2}$

Apel, J. R., Byrne, H. M., Proni, J. R., Charnell, R. L., 1975. Observations of oceanic internal and surface waves from the earth resources technology satellite. Journal of Geophysical Research 80 (6), 865–881.
URL http://dx.doi.org/10.1029/JC080i006p00865

Ardhuin, F., Herbers, T. H. C., Watts, K. P., van Vledder, G. P., Jensen, R., Graber, H. C., 2007. Swell and slanting-fetch effects on wind wave growth. Journal of Physical Oceanography 37 (4), 908–931.
URL https://doi.org/10.1175/JPO3039.1

Babanin, A., Soloviev, Y., 1998. Field Investigation of Transformation of the Wind Wave Frequency Spectrum with Fetch and the Stage of Development. Journal of Physical Oceanography 28 (4), 563–576.

Barber, N. F., 1949. A Diffraction Analysis of a Photograph of the Sea. Nature 164 (485).

Barber, N. F., Dec. 1954. Finding the Direction of Travel of Sea Waves. Nature 174, 1048–1050.

Barrick, D. E., Lipa, B. J., 1985. Mapping surface currents. Sea Technology, 42.

Bolshakov, A. N., Burdyugov, V. M., Grodsky, S. A., Kudryavtsev, V. N., 1988. The spectrum of energy containing surface waves as derived from sun glitter images. Issledovaniye Zemli iz Kosmosa 5, 11–18.

Breon, F. M., Henriot, N., 2006. Spaceborne observations of ocean glint reflectance and modeling of wave slope distributions. Journal of Geophysical

493 Research: Oceans 111 (C6), n/a–n/a, c06005.
494 URL http://dx.doi.org/10.1029/2005JC003343

495 Caudal, G., Hauser, D., Valentin, R., Gac, C. L., 2014. Kuros: A new air-
496 borne ku-band doppler radar for observation of surfaces. Journal of Atmo-
497 spheric and Oceanic Technology 31 (10), 2223–2245.
498 URL https://doi.org/10.1175/JTECH-D-14-00013.1

499 Cox, C., Munk, W., 1954. Measurement of the roughness of the sea surface
500 from photographs of the sun's glitter. Journal of the Optical Society of
501 America (1917-1983) 44, 838.

502 Cox, C., Munk, W., 1956. Slopes of the sea surface deduced from photographs
503 of sun glitter. Bulletin of the Scripps Institution of Oceanography 6 (9),
504 401–488.

505 D'Asaro, E. A., Shcherbina, A. Y., Klymak, J. M., Molemaker, J., Novelli,
506 G., Guigand, C. M., Haza, A. C., Haus, B. K., Ryan, E. H., Jacobs, G. A.,
507 Huntley, H. S., Laxague, N. J. M., Chen, S., Judt, F., McWilliams, J. C.,
508 Barkan, R., Kirwan, A. D., Poje, A. C., Özgökmen, T. M., 2018. Ocean
509 convergence and the dispersion of flotsam. Proceedings of the National
510 Academy of Sciences.
511 URL http://www.pnas.org/content/early/2018/01/09/1718453115

512 Davidan, I. N., 1980. Investigation of wave probability structure on field data.
513 GOIN 151 151, 8–26.

514 De Michele, M., Leprince, S., Thiebot, J., Raucoules, D., Binet, R., 07 2012.
515 Measurement of ocean waves velocity fields from a single spot-5 dataset

using correlation between panchromatic and multispectral bands. Remote Sensing of Environment 199, 266–271.

Dobson, F., Perrie?, W., Toulany, B., 03 1989. On the deep-water fetch laws for wind?generated surface gravity waves. Atmosphere-Ocean 27, 210–236.

Donelan, M., Hamilton, J., Hui, W., 1985. Directional spectra of wind-generated ocean waves. Philosophical Transactions of the Royal Society of London A: Mathematical, Physical and Engineering Sciences 315 (1534), 509–562.
URL http://rsta.royalsocietypublishing.org/content/315/1534/509

Dugan, J., Piotrowski, C., 02 2003. Surface current measurements using airborne visible image time series 84, 309–319.

Ewans, K., C. Kibblewhite, A., 09 1990. An examination of fetch-limited wave growth off the west coast of new zealand by a comparison with the jonswap results. Journal of Physical Oceanography - J PHYS OCEANOGR 20, 1278–1296.

Hennings, I., Matthews, J., Metzner, M., 1994. Sun glitter radiance and radar cross-section modulations of the sea bed. Journal of Geophysical Research: Oceans 99 (C8), 16303–16326.
URL http://dx.doi.org/10.1029/93JC02777

Herbers, T. H. C., Jessen, P. F., Janssen, T. T., Colbert, D. B., MacMahan, J. H., 2012. Observing ocean surface waves with gps-tracked buoys. Journal of Atmospheric and Oceanic Technology 29 (7), 944–959.
URL https://doi.org/10.1175/JTECH-D-11-00128.1

Kahma, K., 10 1981. A study of the growth of the wave spectrum with fetch. Journal of Physical Oceanography 11, 1503–1515.

Kudryavtsev, V., Myasoedov, A., Chapron, B., Johannessen, J. A., Collard, F., 2012. Imaging mesoscale upper ocean dynamics using synthetic aperture radar and optical data. Journal of Geophysical Research: Oceans 117 (C4), n/a–n/a, c04029.
URL http://dx.doi.org/10.1029/2011JC007492

Kudryavtsev, V., Myasoedov, A., Chapron, B., Johannessen, J. A., Collard, F., 2012. Joint sun-glitter and radar imagery of surface slicks. Remote Sensing of Environment 120 (Supplement C), 123 – 132, the Sentinel Missions - New Opportunities for Science.
URL http://www.sciencedirect.com/science/article/pii/S0034425712000831

Kudryavtsev, V., Yurovskaya, M., Chapron, B., Collard, F., Donlon, C., 2017a. Sun glitter imagery of ocean surface waves. Part 1: Directional spectrum retrieval and validation. Journal of Geophysical Research: Oceans 122 (2), 1369–1383.

Kudryavtsev, V., Yurovskaya, M., Chapron, B., Collard, F., Donlon, C., 2017b. Sun glitter imagery of surface waves. Part 2: Waves transformation on ocean currents. Journal of Geophysical Research: Oceans 122 (2), 1384–1399.

Lupyan, E. A., 1988. Retrieval of the angular energy distribution of two-dimensional elevation spectrum from optical image of the sea surface. Issledovaniye Zemli iz Kosmosa 3, 31–35.

Lygre, A., Krogstad, H. E., 1986. Maximum entropy estimation of the directional distribution in ocean wave spectra. Journal of Physical Oceanography 16 (12), 2052–2060.
URL https://doi.org/10.1175/1520-0485(1986)016<2052:MEEOTD>2.0.CO;2

Melville, W. K., Lenain, L., Cayan, D. R., Kahru, M., Kleissl, J. P., Linden, P. F., Statom, N. M., 2016. The modular aerial sensing system. Journal of Atmospheric and Oceanic Technology 33 (6), 1169–1184.
URL https://doi.org/10.1175/JTECH-D-15-0067.1

Monaldo, F. M., Kasevich, R. S., 1981. Daylight imagery of ocean surface waves for wave spectra. Journal of Physical Oceanography 11 (2), 272–283.
URL https://doi.org/10.1175/1520-0485(1981)011<0272:DIOOSW>2.0.CO;2

Nieto, B., Rodrigues, G., Hessner, K., Gonsalez, B., 2004. Inversion of marine radar images for surface wave analysis. Journal of Atmospheric and Oceanic Technology 21, 1291–1300.

Rascle, N., Molemaker, J., Mari?, L., Nouguier, F., Chapron, B., Lund, B., Mouche, A., 2017. Intense deformation field at oceanic front inferred from directional sea surface roughness observations. Geophysical Research Letters 44 (11), 5599–5608, 2017GL073473.
URL http://dx.doi.org/10.1002/2017GL073473

Rascle, N., Nouguier, F., Chapron, B., Mouche, A., Ponte, A. l., 2016. Surface roughness changes by finescale current gradients: Properties at multiple azimuth view angles. Journal of Physical Oceanography 46 (12), 3681–3694.

585 Senet, C. M., Seeman, J., Flampouris, S., Ziemer, F., 2008. Determination
586 of Bathymetric and Current Maps by the Method DiSC Based on the
587 Analysis of Nautical X-Band Radar Image Sequences of the Sea Surface.
588 IEEE Transactions on Geoscience and Remote Sensing 46 (8), 2267–2279.

589 Spooner, J., 1822. Sur la lumiere des ondes de la mer. Corresp. Astronomique
590 du Baron de Zach 6, 331.

591 Stilwell, D., 1969. Directional energy spectra of the sea from photographs.
592 Journal of Geophysical Research 74 (8), 1974–1986.
593 URL http://dx.doi.org/10.1029/JB074i008p01974

594 Stilwell, D., Pilon, R. O., 1974. Directional spectra of surface waves from
595 photographs. Journal of Geophysical Research 79 (9), 1277–1284.
596 URL http://dx.doi.org/10.1029/JC079i009p01277

597 Walsh, E. J., Vandemark, D. C., Friehe, C. A., Burns, S. P., Khelif, D., Swift,
598 R. N., Scott, J. F., 1998. Measuring sea surface mean square slope with a
599 36-ghz scanning radar altimeter. Journal of Geophysical Research: Oceans
600 103 (C6), 12587–12601.
601 URL http://dx.doi.org/10.1029/97JC02443

602 Wen, S. C., Zhang, D. C., Guo, P. Z., Chen, B. H., 1989. Parameters in
603 wind?wave frequency spectra and their bearings on spectrum forms and
604 growth. Acta Oceanol. Sinica 8, 15–39.

605 Yurovskaya, M., Kudryavtsev, V., S. Shirokov, A., Yu. Nadolya, I., 01
606 2018. Field measurements of the sea surface wave spectrum from pho-

607 tos of sunglitter taken from drone. Sovremennye problemy distantsionnogo
608 zondirovaniya Zemli iz kosmosa 15, 245–257.

609 Yurovsky, Y. Y., Kudryavtsev, V. N., Grodsky, S. A., Chapron, B., 2018.
610 Low-frequency sea surface radar doppler echo. Remote Sensing 10 (6).

List of Figure Captions

Figure 1

(a) The observation area with NDBC buoy locations (gray diamonds). Green star shows location of the analysis on 11-Feb-2016 (section 4), colors are the tracks of the 23-Jan-2016 flight (section 5). (b) Sketch of the field of view of the afterward camera, for a flight altitude of 1000 m. Here we show the special case of the sun exactly at the rear of the airplane when the specular sun spot is at the center of the camera field of view. The ellipse is the contour $Z_n^2 = s^2$ (see the notifications below). The white arrows show the orientations of the transfer function gradient, G_{zi}.

Figure 2

(a) An airborne snapshot of a sea surface; (b) image projected on the sea surface plane (x-label is to the East, y-label is to the North, two ellipses determine the zone $0.5 < Z_n^2/s^2 < 2$); (c) pixel intensities for the left column of a photo (dots) and their polynomial approximation indicating the background radiation; (d) $\cos\theta/\rho$ field; (e) $B = (N - N_{back})\cos\theta/\rho$ field; (f) mean brightness field, B_0

Figure 3

(a) Square fragments (450 m size) of brightness variation field, $(B-B_0)$, taken for spectrum retrieval. Two ellipses determine the zone $0.5 < Z_n^2/s^2 < 2$, black line is $\theta = 50°$; (b) The sum of brightness spectra; (c) the transfer function, $\sum_{n=1}^{N}(G_{zi}^n k_i)^2$; (d) retrieved from (6) elevation spectrum; (e) NDBC buoy data directional spectrum (42012); (f) Omnidirectional spectra comparison.

Figure 4

(a)-(b) Snapshots of the same location taken with 0.5 s time shift; (c) coherence of two brightness fields; (d) phase shift; wave direction (from) corresponds to positive values of a phase shift; (e) dispersion relation calculated from a phase shift along the line of coherence maximum (dashed lines in (c) and (d) plots).

Figure 5

Locations of the images acquired on 23-Jan-2016 near NDBC buoys 42012 and 42040, and schematic wave systems orientations.

Figure 6

Windspeed, wind direction and directional slope spectra from NDBC 42012 and 42040 buoys around the time of airplane flight. Wind and wave directions are ‘’from” in nautical system.

Figure 7

Directional slope spectra at the points marked by red squares on fig 5. White line is the wind direction from buoy data (trigonometrical system). Spectrum develops in presence of swell from West. Wind wave peak grows and shifts towards low wavenumbers, slightly deviates from NDBC wind direction (actually the wind also changed its direction).

Figure 8

Omnidirectional spectra at the points marked by red squares on fig 5. Wind peak grows and shifts towards lower wavenumbers in consistence with Donelan et al. (1985) and Babanin and Soloviev (1998) spectra. Blue (Babanin and Soloviev, 1998) and green (Donelan et al., 1985) curves are given for the wind speed taken from the nearest buoy (42012 or 42040) and the fetch is corrected accounting for the spectrum wind wave peak direction estimated

from Fig. 7.

Figure 9

(a) Dimensionless peak frequency vs. dimensionless fetch. Black circles – experimental points (all retrieved spectra), dashed lines – approximations from other authors (Davidan, 1980; Babanin and Soloviev, 1998; Donelan et al., 1985; Kahma, 1981; Dobson et al., 1989; Wen et al., 1989; Ewans and C. Kibblewhite, 1990) for the wind speed 9 m s^{-1}; (b) Dimensionless peak frequency vs. windsea demensionless variance with the same notations; (c) angular function suggested by Donelan et al. (1985) and ensemble average wave energy distribution around the peak wavenumber ($0.75k_p < k < 1.25k_p$); the length of vertical lines is equal to standard deviation.

Figure 10

Left: the longest waves which can be observed within the useful part of the sunglint ($0.5 < Z_n^2/s^2 < 2$), as function of the camera altitude H. Three different sun zenith angles ($\theta_s = 15, 30, 45^o$) and three different wind speeds ($5, 10, 15$ m s^{-1}) are used for the calculations. Right: surface resolution as a function of camera altitude for the image size $N_p = 1000$ pixels, different camera view angles and two camera zenith angles ($\theta = 0^o$ and $\theta = 50^o$)